공학석사 학위논문

Gyrotropic Motions in One-dimensional Magnetic Vortex-Antivortex Lattices

1 차원 자기 소용돌이-반소용돌이 격자에서 발생하는 회전운동에 관한 연구

2015 년 2 월

서울대학교 대학원

공과대학 재료공학부

정한별

Gyrotropic Motions in One-dimensional Magnetic Vortex-Antivortex Lattices

A THESIS
SUBMITTED TO THE FACULTY OF SEOUL NATIONAL UNIVERSITY
BY

Han-Byeol Jeong

Supervised by

Prof. Sang-Koog Kim

IN PARTIAL FULFILLMENT OF
THE REQUIREMENTS FOR THE DEGREE OF MASTER

February 2015

Department of Material Science and Engineering

Graduate School

Seoul National University

Gryotropic Motions in One-dimensional Magnetic Vortex-antivortex lattices

지도교수 김 상 국

이 논문을 공학석사 학위논문으로 제출함

2015년 2월

서울대학교 대학원

재 료 공 학 부

정 한 별

정한별의 석사학위 논문을 인준함

2015년 2월

위 원 장 김 미 영 (인)

부 위 원 장 김 상 국 (인)

위 원 한 승 우 (인)

Abstract

Gyrotropic Motions in One-dimensional Magnetic Vortex-Antivortex Lattices

Han-Byeol Jeong

Department of Materials Science and Engineering

Seoul National University

Recently, as a potential candidate of next-generation signal-transfer device, the dynamics of coupled magnetic vortices have been studied. One of the required features of future devices is high working speed, but the previous results of signal-transfer speed of an array of separated vortex disks were relatively lower than other candidates.

In this thesis, we introduced the connected disks structure, where a magnetic vortex and antivortex are formed in turn. They are strongly coupled via not only a long-range dipole-dipole interaction, but also a short range exchange interaction. We observed the signal transfer phenomena by way of gyration propagation of the coupled vortex-antivortex array, and revealed that the collective oscillations of the cores' gyration were decomposed by fundamental modes, described as standing waves. In addition, we found two unique branches of band structures, which imply that the dynamics of the vortex-antivortex array acts as the diatomic lattice vibration.

We also demonstrated the control of gyration propagation speed by application of a perpendicular magnetic field. The gyration propagation speed for the parallel polarization ordering is much faster (>1 km/s) than that for the 1D vortex-state arrays.

This work provides a fundamental understanding of the coupled dynamics of topological solitons, as well as an additional mechanism for fast gyration-signal propagation; moreover, it offers an efficient means of significant propagation-speed enhancement that is suitable for information carrier applications in continuous thin-film nanostrips.

Keywords: magnetic vortex, magnetic antivortex, magnonic crystal, signal transfer

Student number: 2012-23152

Contents

List of Figures

Chapter 1

Introduction

Over the last few decades, the development of semiconductor devices has led to the tremendous advancement of modern information society. The strategy of the development of semiconductor technology is to “scale down”. Nowadays, the line width of semiconductor devices is typically reduced by ~10nm, but the highly integrated devices are facing limitations in development in areas such as high leakage current and large heat dissipation. [1]

The essential reason of the limitation of future semiconductor devices is that the working process is based on the movement of electrons, a charged particle. Therefore spin-based devices as a non-charge based device, such as race-track memory, which utilize magnetic domain wall motion [2], spin-transfer torque magnetic random access memory (STT-MRAM)[3] and spinwave devices [4-6], have been studied owing to the potential implementation of information processing devices with faster working speed and lower power consumption.

In particular, spinwaves, the collective motion of individual spins, has attracted increasing attention as a source of information processing. It is a purely non-particle based energy transfer mechanism, free of the Joule heating problem that spintronic devices still have. Spinwaves, excited in nanostructures are

promising due to fast propagation speed (~km/s) and very short wavelength [7]. But, it is hard to detect a spinwaves' signal due to its small variation of magnetization. As an alternative, magnetic vortexes, which have curling magnetization structure usually formed in micro~nanopatterned soft-magnetic material, have been widely studied. Magnetic vortexes have intriguing gyration dynamics [8,9], and the consequential large variation of magnetization gives rise to reliable signal detection [10, 11]. In addition, magnetic vortexes show another type of interesting dynamic behavior, core-switching [12, 13]. These unique characteristics of magnetic vortex allow for their potential application for information-storage [14, 15] and processing [16-18], as well as usage as microwave devices [11, 19, 20].

The signal transfer phenomenon using a magnetic vortex is achieved by coupled vortices. It is known that collective gyrotropic motions of coupled vortices are similar to the dynamics of coupled harmonic oscillator [21]. It was subsequently demonstrated that signal transfer is possible via the vortex gyration propagation in the array of magnetic vortexes. Even though signal transfer via vortex gyration propagation provides easy detection of the output signal, the reported propagation speeds [22 - 24] were relatively lower (< 1km/s) than that of spinwaves in nanostructure. The previous studies of signal transfer in vortex array were focused on the array of physically isolated disks. Therefore, the mutual interaction between neighboring disks were mediated only by long-range dipole-dipole interaction.

In this thesis, we deal with physically connected disks structure, where magnetic vortex and antivortex are formed in turn. The magnetic antivortex is the topological counterpart of the vortex, and has been found to exhibit core gyration and related switching behaviors similar to vortex dynamics [25-27]. Isolated antivortices, due to their unstable state, can possibly be formed in specially designed geometric confinements [25-31]. On the other hand, periodic vortex and antivortex arrangements have often been found as parts of cross-tie walls [28,32].

Although the dynamics of single antivortices [25-27] and their dynamic interactions with vortices [20, 33-35] have been reported in earlier studies, the dynamics of coupled vortices and antivortices in round-shaped modulated nanostrips and their coupled gyration propagation have not been well understood in the magnonic band aspect or in terms of gyration-signal propagations through 1D alternating vortex-antivortex (V-AV) lattices.

We report on the collective dynamic behaviors of interacting vortices and antivortices in 1D periodic V-AV lattices, specifically in terms of their coupled excitation modes, notably unique band structures, and gyration-signal propagation speed. In chapter 2, we provide the research background including both theoretical background and introduction of magnetic vortex and antivortex. In chapters 3 and 4, we deal with coupled motion of vortex-antivortex in a finite array and semi-infinite array. Finally, the summary of the thesis is in chapter 5.

Chapter 2

Research background

2.1 Micromagnetics

Prior to the discussion on the dynamic properties of vortex and antivortex, we briefly deal with micromagnetics, a continuum theory that thoroughly explains static and dynamic problems of magnetization at the mesoscale (sub-micrometer length scale) dimension. Micromagnetics, mainly developed by W. F. Brown, Jr. [36], now have become a powerful tool that predicts statics and dynamics spin phenomena by means of the rapid development of computation power.

The dynamics of magnetization (**M**) can be described by the LLG equation, first introduced by Landau and Lifshitz in 1935 [37] and modified by Gilbert in 1955 [38]. The LLG equation is expressed as

$$\frac{d\mathbf{M}}{dt} = -\gamma \mathbf{M} \times \mathbf{H}_{eff} + \frac{\alpha}{M_s} \mathbf{M} \times \frac{d\mathbf{M}}{dt} \quad (2.1)$$

where γ is the gyromagnetic ratio, $\mathbf{H}_{eff}$ is the effective field, α is the Gilbert damping constant, and M_s is the saturation magnetization. The first term on the right-hand side (RHS) make the precession motion of magnetization, and the

second term on the RHS is related to the damping process, which causes magnetization to align along the effective field, as shown in Fig 2.1.

The effective field ($\mathbf{H}_{\text{eff}}$) is expressed as a derivative of total energy with respect to magnetization.

$$\mathbf{H}_{eff} = \frac{\partial E}{\partial \mathbf{M}} \quad (2.2)$$

Total energy involves four distinct interactions: Zeeman, exchange, magnetostatic, and magnetocrystalline anisotropy, interaction represent the interaction between magnetization and the external magnetic field.

In ferromagnetic material, exchange interaction, originating from the quantum mechanical effect between identical particles, favors the parallel spin configuration. Under the assumption that the angle difference between the neighboring spin is small, the exchange energy is expressed as

$$E_{ex} = \int_V A_{ex}[(\nabla m_x)^2 + (\nabla m_y)^2 + (\nabla m_z)^2]\, dV \quad (2.3)$$

where A_{ex} is the exchange constant and (m_x, m_y, m_z) are components of normalized magnetization ($\mathbf{M}/M_s$). In the Heisenberg model, A_{ex} is given as JS^2/a, where J is

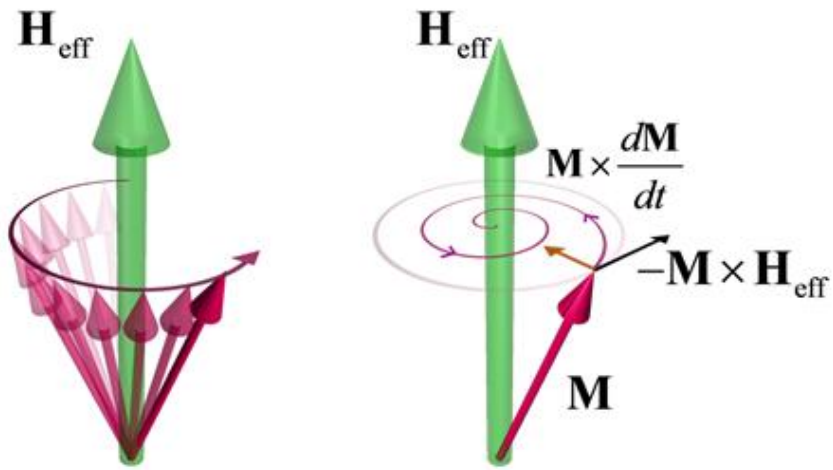

Fig. 2.1 Schematic illustration for the precession and damping motion of magnetization (**M**) under the effective field ($\mathbf{H}_{\mathrm{eff}}$). [39]

the exchange integral, *S* is an atomic spin, and *a* is the lattice constant.

Magnetostatic energy, also known as demagnetization energy, arises from dipole-dipole interaction among individual spins. From the Maxwell equation, magnetostatic energy involves two types of magnetic charge (magnetic surface charge and magnetic volume charge). Furthermore, magnetostatic interaction prefers to minimize the two magnetic charges. Generally, the magnetic field generated by dipoles reduces the magnetization of the sample. We call the field a "demagnetization field". Magnetostatic energy is given by

$$E_{ms} = \int_V -\frac{1}{2}\mathbf{M}\cdot\mathbf{H}_d \, dV \quad (2.4)$$

where $\mathbf{H}_d$ is the demagnetization field.

In real ferromagnetic material, anisotropic spin-orbit coupling caused by the crystal structure gives rise to the preferential direction of magnetization, called an easy axis. Therefore, the equation of magnetocrystalline anitropy energy depends on the crystal structure. For instance, in the case of Fe of cubic system with <100> easy axis, the equation of the magneto crystalline energy is given as follows:

$$E_a / V = K_0 + K_1(\alpha^2\beta^2 + \beta^2\gamma^2 + \gamma^2\alpha^2) + K_2(\alpha^2\beta^2\gamma^2) \quad (2.5)$$

where K_0, K_1 and K_2 are anisotropy constants depending on material, (α, β, γ) are directional cosines of magnetization with respect to the easy axis, and *V* is a total

volume. However, we note that permalloy ($Ni_{80}Fe_{20}$), the material used in the thesis has zero anisotropy constant, therefore we did not consider magnetocrystalline anisotropy energy.

Finally, Zeeman energy is the potential energy of magnetization in an external field.

$$E_H = \int_V -\mathbf{M} \cdot \mathbf{H}_{ext} dV \quad (2.6)$$

2.2 Micromagnetic simulation

Micromagnetic magnetic simulation provides a numerical solution of the LLG equation, so that it enables us to predict magnetization dynamics without experiments. Furthermore, the resolution of micromagnetic simulation is determined by the cell-size from ~nm to subnanometer scale. Therefore, micromagnetic simulations also provide high resolution data that cannot be obtained by experiment yet. Up to now, many free and commercial micromagnetic simulators have been released. In this thesis, Object oriented micromagnetic framework (OOMMF)[40], the most popular open source code, was utilized.

2.3 Magnetic vortex and antivortex

Magnetic vortex is a unique magnetic structure found in submicron-sized ferromagnetic element, where the dominant energy competition between exchange interaction and dipole-dipole interaction exist. Exchange interaction prefers parallelspin configuration, whereas dipole-dipole interaction favors closure spin configuration to reduce magnetic free pole. As a result, the magnetic vortex has a peculiar spin configuration with in-plane curling magnetization and out-of plane magnetization (vortex core) within a local region of ~10nm as shown in Fig. 2.2.

In the meantime, magnetic antivortex is also a kind of curling magnetic configuration with its local out-of plane magnetization (antivortex core) as shown in Fig. 2.3. Fig. 2.4 shows the in-plane spin configuration of magnetic vortex and antivortex. The angle of in-plane magnetization, ϕ, can be expressed as $\phi = n\beta + \pi c/2$, where n is winding number, β is the angle of position vector of a given magnetization, and c is chirality [21]. The winding number of vortex and antivortex are 1 and -1. Therefore the direction of in-plane magnetization of vortex turns counterclockwise as the β increases, but vice versa for antivortex. Chirality c is determined by the angle of magnetization on the $+x$ axis, and indicates the phase of spin configuration. In the case of vortex, chirality c represents the rotation of in-plane magnetization. $c = 1$ ($c = -1$) corresponds counterclockwise (clockwise) rotation sense of in-plane magnetization. In the case of antivortex, c is a real number within $-2 < c <= 2$. The direction of out-of plane magnetization of vortex

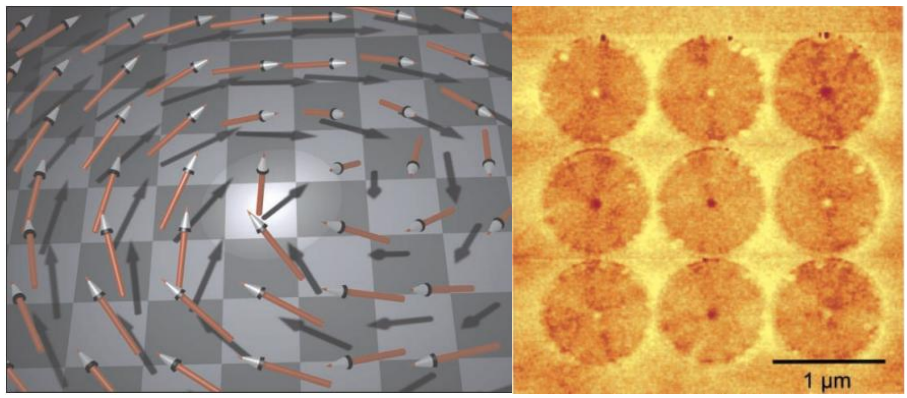

Fig. 2.2 (Left) Schematic spin configuration of magnetic vortex, the highlighted region in the center of figure represents the vortex core[41]. (Right) Magnetic vortex observed by magnetic force microscopy (MFM)[42].

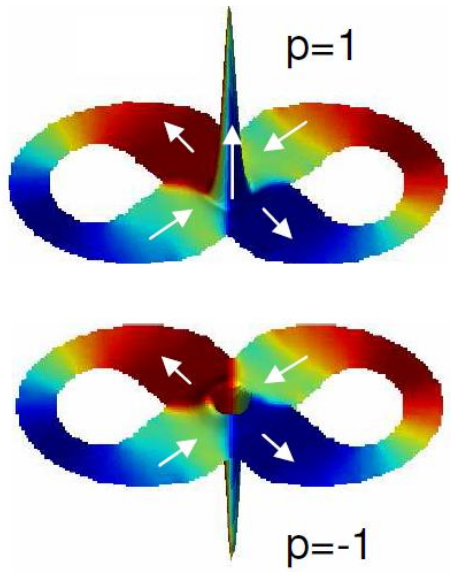

Fig. 2.3 Magnetization structure of antivortex formed in an infinity shape sample [43]. The height indicate the out-of-plane component of magnetization. White arrows indicate the direction of local magnetizations.

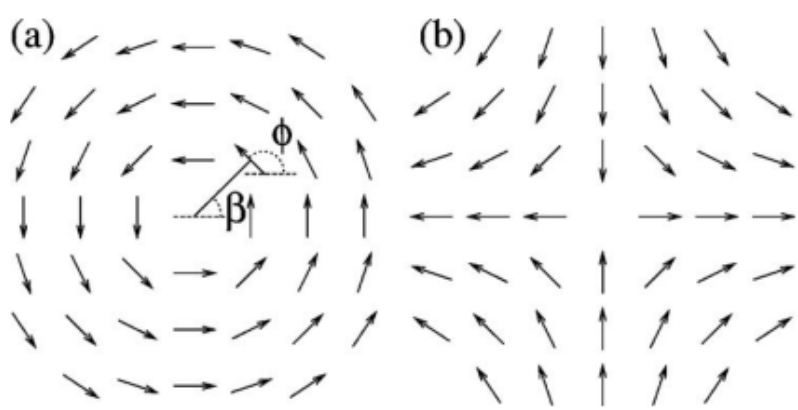

Fig. 2.4 The schematic in-plane spin configuration of (a) vortex and (b) antivortex. [21]

and antivortex is called polarization (p), p = 1 (p = -1) corresponds up (down). Therefore, there are four energetically equivalent states in the vortex system (See Fig. 2.5).

The magnetic vortex and flux closure-state is often found in ground state. Usually, vortex state is formed in sub-micron size soft magnetic disk. However, magnetic antivortex is not flux-closure magnetization, and generates its own strayfield, which increases the unstabillity of the antivortex. The characteristics of the antivortex make it difficult to form a single antivortex state [31]. Therefore, a single antivortex can usually be formed in a specially designed geometric confinement as shown in Fig 2.6.

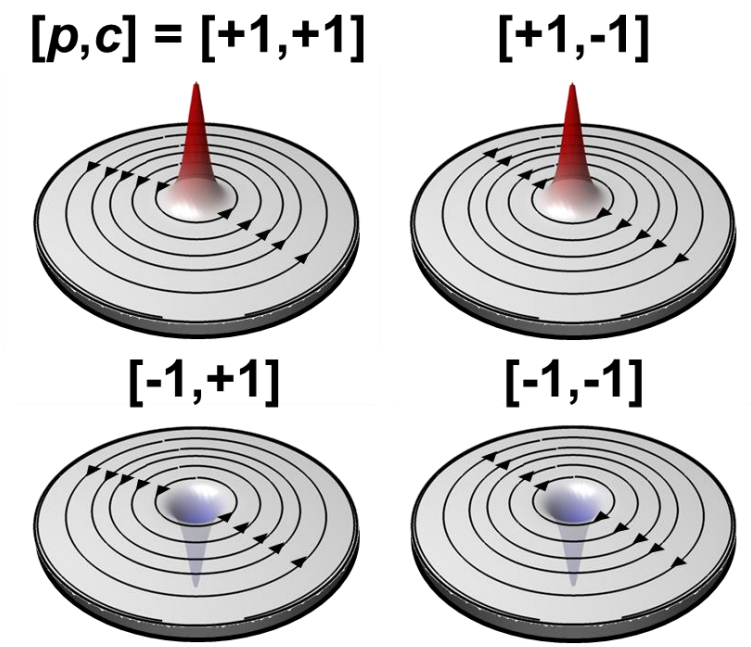

Fig. 2.5 Four energetically equivalent states in the vortex system [39]. The color and height represent the out-of-plane magnetization components (vortex core). The streamlines indicate the in-plane magnetization components.

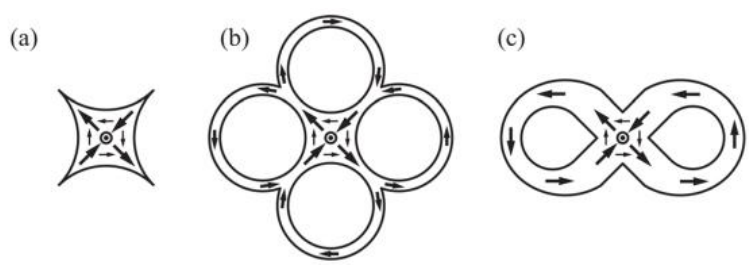

Fig. **2.6** Artificially designed structure to stabilize single antivortex. (a) star-like shape, (b) clover-shape, and (c) infinity-shape [29].

2.4 Gyrotropic mode of magnetic vortex and antivortex

The gyrotropic mode is a unique spin excitation mode of the magnetic vortex and antivortex. In the gyrotropic mode, the (anti)vortex core rotates around the equilibrium position along the potential well. Their motion can be described by Thiele's equation [44, 45], the equivalent force balance equation derived from LLG equation as shown below.

$$-\mathbf{G} \times \frac{d\mathbf{X}}{dt} - D\frac{d\mathbf{X}}{dt} + \frac{\partial W}{\partial X} = 0 \quad (2.7)$$

$\mathbf{X}=(X,Y)$ is the position vector of (anti)vortex core, $\mathbf{G}$ is gyrovector, D is the diagonal dissipation tensor, and W is the potential energy function. The first term of LHS represents the gyroscopic force, and the gyrovector is given by

$$\mathbf{G} = -\frac{2\pi pnM_s}{\gamma}\hat{\mathbf{z}} \qquad \mathbf{(2.8)}$$

where $\hat{\mathbf{z}}$ is out-of plane unit vector. The second term of LHS represents the damping force. The value of each component of diagonal dissipation tensor is $D_{xx} = D_{yy} = D_0, D_{zz} = 0$ where D_0 depends on the sample geometry [21]. The third term represents the restoring force due to a potential well. For small excitation, the potential function of both vortex and antivortex can be expressed as a harmonic potential with the stiffness coefficient κ. [43]

$$W = \tfrac{1}{2}\kappa(X^2 + Y^2) \quad (2.9)$$

Fig 2.7 shows a typical example of the gyrotropic motion of the vortex core [39]. When the static in-plane field is applied in the vortex, the vortex core is displaced from the original equilibrium position. Upon turning off the in-place field, the vortex core starts to gyrate around the original equilibrium center and approaches the center due to damping force. The rotation sense of vortex core gyration is determined by its polarity, which determines the direction of the gyrovector. As shown in Fig 2.6 (b), when vortex core magnetization is upward (downward), or in other words, the polarity is +1 (-1), the rotation sense of the vortex core gyration is counter-clockwise (clockwise).

Fig. 2.8 shows the trajectories of gyrotropic motion of the antivortex core [25]. Unlike the vortex case, when the antivortex core magnetization is upward (downward), the rotation sense of vortex core gyration is clockwise (counter-clockwise). As mentioned earlier, the sign of winding numbers (n) of vortex and antivortex are opposite (n = 1 for vortex, -1 for antivortex). Therefore, the direction of their gyrovectors is also opposite when their polarity is the same. This gives rise to opposite rotation sense between the vortex and the antivortex.

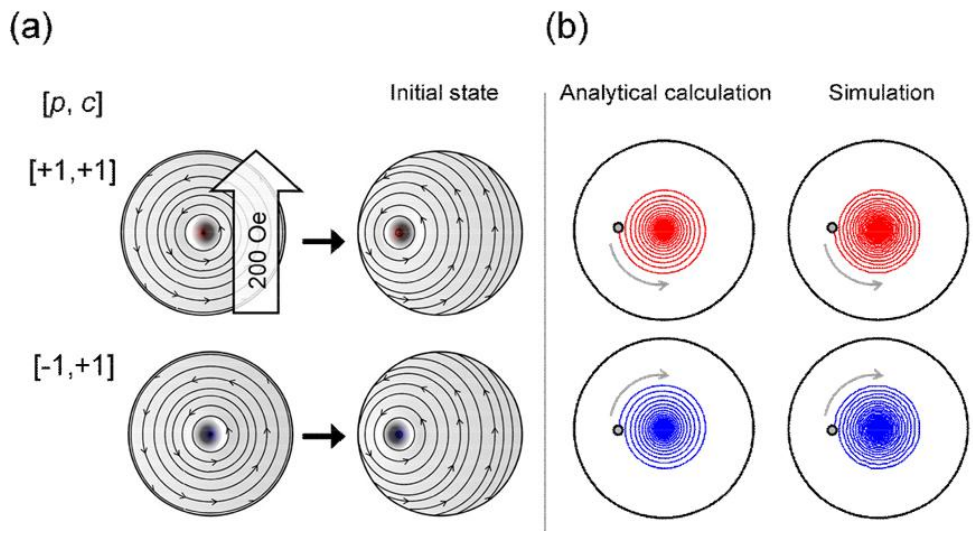

Fig 2.7 The gyrotropic motion of the vortex core from the initial state where the vortex core is displaced from the equilibrium state. (a) The initial state is changed by applying the static inplane field. (b) Gyrotropic motion of vortex core under free relaxation obtained by analytic calculation (left) and simulation (right) [39]

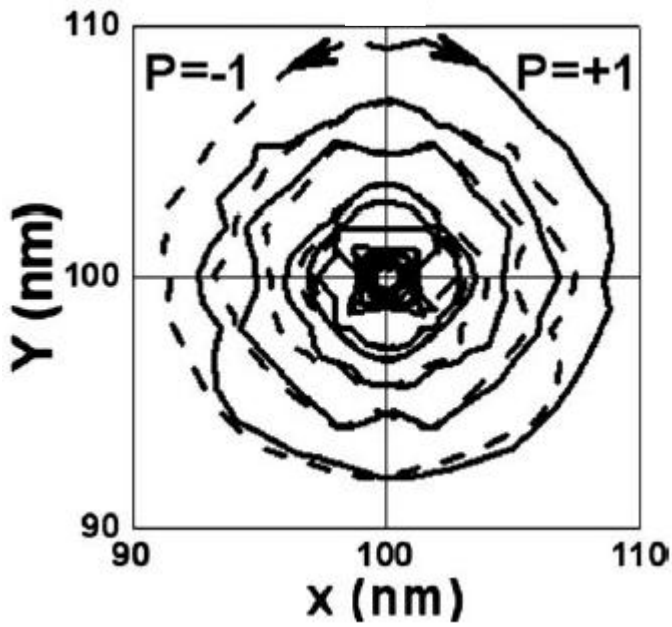

Fig. 2.8 Trajectories of the gyrotropic motion of antivortex core. [30] Clockwise (counter-clockwise) path is for p=+1 (p=-1).

2.5 Coupled system of vortices and antivortices

Magnetic vortex and antivortex generate strong stray fields when the (anti)vortex core is displaced from the equilibrium position. Therefore, more interesting dynamic behavior of the two vortex pairs or periodically arranged vortex arrays appear compared to that of a single vortex due to their magnetostatic interaction. Shibata *et al*. [46] reported on magnetostatic energy between two separated vortex disks, which can be expressed as

$$W_{\mathrm{int}} = C_1 C_2 (\eta_x X_1 X_2 - \eta_y Y_1 Y_2)$$

where C_1 and C_2 is chirality of the first and second vortex, η_x and η_y are the inreaction strengths along the x and y axis.

The coupled gyration of the vortex pair was first observed by Jung *et al.* [47], by using magnetic transmission soft x-ray microscopy (MTXM). Vogel *et al.* [48] demonstrated a signal transfer by coupled vortex gyration. Systematic study of collective modes of vortex gyration in the one-dimensional vortex array was achieved by Han *et al*.[49]. Collective vortex gyration of 5 element array was experimentally observed by MTXM. Each collective mode in the finite vortex array could be expressed as a standing wave interpretation. Also, in the case of semi-infinite vortex array, the dispersion relation of collective vortex gyration is strongly affected by chirality and polarization ordering.

In the case of an antivortex, due to the complex sample design of the

isolated antivortex, it is difficult and inappropriate to study the array of isolated antivortexes. Usually, a set of antivotices is formed in a part of cross-tie domain wall [28, 32]. Fig 2.9 (a) shows the schematic structure of a cross-tie domain wall [50]. In the cross-tie wall, an antivortex is formed between vortices of the same chirality. Shigeto *et al*. [32] observed a MFM image of cross-tie wall in permalloy thin film (Fig 2.9 (b)) and detected vortex and antivortex cores in the cross-tie wall. Magnetic vortex antivortex can be formed by means of magnetocrystalline anisotropy. J. Li *et al*. [51] demonstrated the formation of ground state of vortex-antivortex array in expitaxial Fe/Ag film.

In the meantime, Kuepper *et al*. [33] reported the magnetization dynamics of coupled vortex-antivortex in a single cross-tie wall by measurement of time-resolved. They revealed that not only was the coupling of vortex and antivortex in cross-tie wall mediated by exchange interaction of the adjacent domain walls, but also the polarity configuration dependent eigenmodes of coupled vortex-antivortex gyration, as well.

To sum up, the previous studies of coupled vortices was mainly focused on the array of separated vortices. From the point of view of application, such as in the case of information processing devices, only dipolar coupled vortices would have a limitation in terms of interaction strength. In this case, a coupled vortex-antivortex array that is physically connected can serve as a solution to the problem because their dynamics involve not only dipolar interactions but also strong exchange interactions. However, the dynamics of coupled vortices and antivortices

and their coupled gyration propagation have not been well understood.

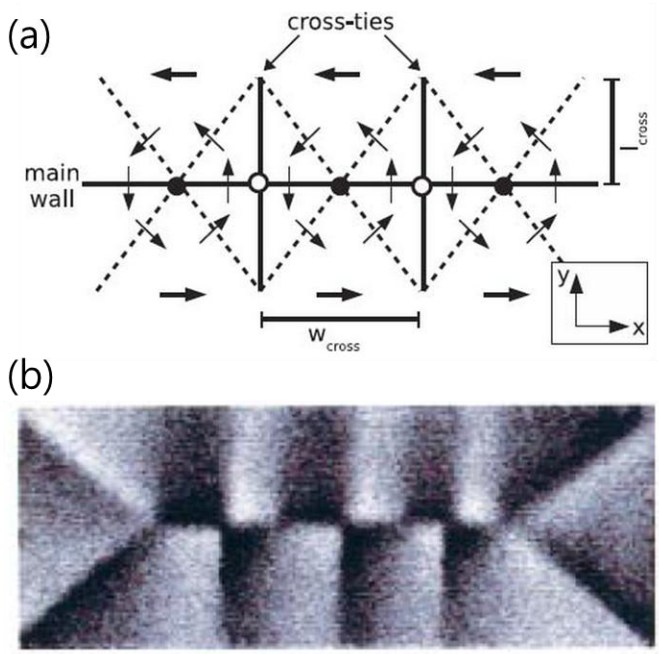

Fig 2.9 (a) Schematic illustration of a cross-tie domain wall[50]. Solid (open) circle represent vortex (antivortex) core. (b) MFM image of cross-tie wall[28].

Chapter3

Collective modes of vortex-antivortex gyration in 1D finite vortex-antivortex lattices.

We designed finite vortex-antivortex array, metastably formed in connected disks structure. Fundamental eigenmodes of the vortex-antivortex array were explored by local excitation of the vortex core. From inverse fast Furrier transformation of the each eigenmode peak in the frequency spectra, spatial correlation of each eigenmode was obtained.

3.1 Simulation condition

In the present study, we used, for a model system, alternating V-AV lattices in a connected triple-disk structure wherein the diameter of each disk is $2R$ = 303 nm, the thickness T = 20 nm, and the center-to-center interdistance D_{int} = 243 nm, for cases of $R < D_{int} < 2R$ (see Fig. 3.1). Unlike physically separated disks (i.e., $D_{int} > 2R$), this connected triple-disk structure has two antivortices between neighboring vortices of the same counter-clockwise (CCW) chirality in a sufficiently stable metastable state. The geometrical parameters used here were optimized to achieve vortex and antivortex arrays in at least metastable states, thereby allowing coupled core gyrations to propagate well along the chains. When D_{int} becomes longer, it is difficult to form antivortices and their gyrations; whereas when D_{int} becomes shorter, the neighboring vortices and antivortices are in too-close proximity, so that they might be annihilated during their coupled gyrations. In the initial state, the core magnetizations of the three vortices are upward (called polarization p = +1), and those of the two antivortices are downward (p = -1), resulting in the antiparallel polarization ordering. We numerically calculated the motions of local magnetizations (cell size: $3\times3\times T$ nm^3) using the OOMMF code[40]. We used the typical material parameters of Permalloy ($Ni_{80}Fe_{20}$, Py): saturation magnetization M_s=8.6×10^5 A/m, exchange stiffness A_{ex}= 1.30×10^{-11} J/m, and zero magnetocrystalline anisotropy.

To excite all of the coupled modes in such a model system, we displaced

the core only of the left-end disk up to ~54 nm in the $-x$ direction by applying a static local field of 200 Oe in the $+y$ direction. Upon turning off the local field, the five individual cores of the vortices and antivortices were monitored to trace the trajectories of the coupled core motions. All of the simulation time was 200ns.

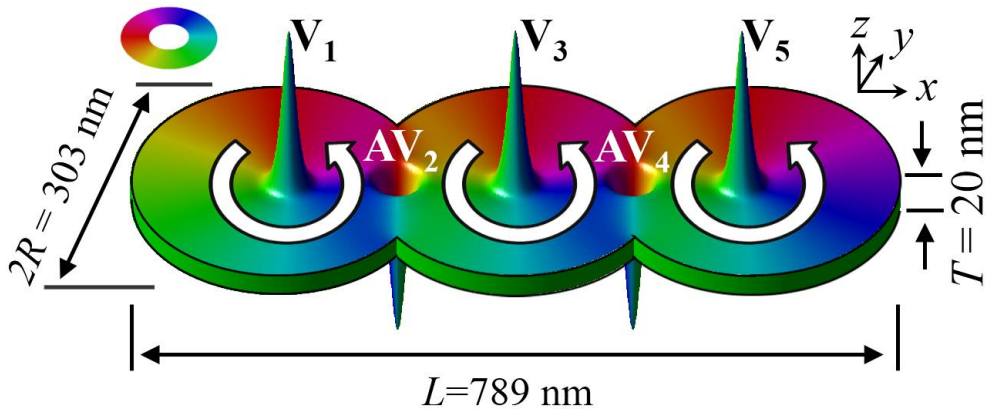

Fig. 3.1 Model geometry of connected triple-disk structure (round-shaped modulated nanostrip). The individual disks have an equal diameter $2R$ = 303nm, a thickness T = 20 nm, and a disk center-to-center distance D_{int} = 243 nm. The color and height display the in-plane magnetization and out-of-plane magnetization components, respectively. The chirality of the three vortices is CCW, as indicated by the white arrows, and the polarizations of the three vortices and two antivortices are upward and downward, respectively.

3.2 Vortex-antivortex core gyration propagation and eigenmode frequencies

Fig. 3.2 shows temporal changes of vortex cores antivortex core after the relaxation. Firstly V1, shifted by the initial magnetic field moved, and the motion of V_1 induced the motion of neighboring cores(AV_2). This process repeated from V_1 to V_5, therefore this result reveals that signal transfer is possible by gyration propagation of magnetic vortex-antivortex lattices. Fig. 3.3 (a) shows the individual trajectories of coupled core gyrations with their position vectors **X**= (*X*, *Y*). Owing to direct excitation of the core in the first disk (noted as V_1), a large amplitude of gyration toward the center position, starting at *X*= - 54 nm, is observed. The vortex gyration of the first disk is then propagated to the next antivortex (AV_2), and then further propagates through the whole system, as evidenced by the large gyration amplitudes of the remaining vortices, indicated as V_3 and V_5. These large gyration amplitudes imply that the vortex gyration is well transferred (propagated) to the next vortices through the neighboring antivortices, with negligible energy loss. To elucidate the observed modes, we plotted, in the left column of Fig. 3.3 (b), the frequency spectra of the individual core motions as obtained from fast Fourier transformations (FFTs) of the *x* components of the individual core oscillations. From the first vortex to the last one, contrasting FFT powers between the major five peaks are observed. The distinct peaks are denoted ω_i, with i = 1, 2, 3, 4, and 5. The individual peaks in the frequency domains

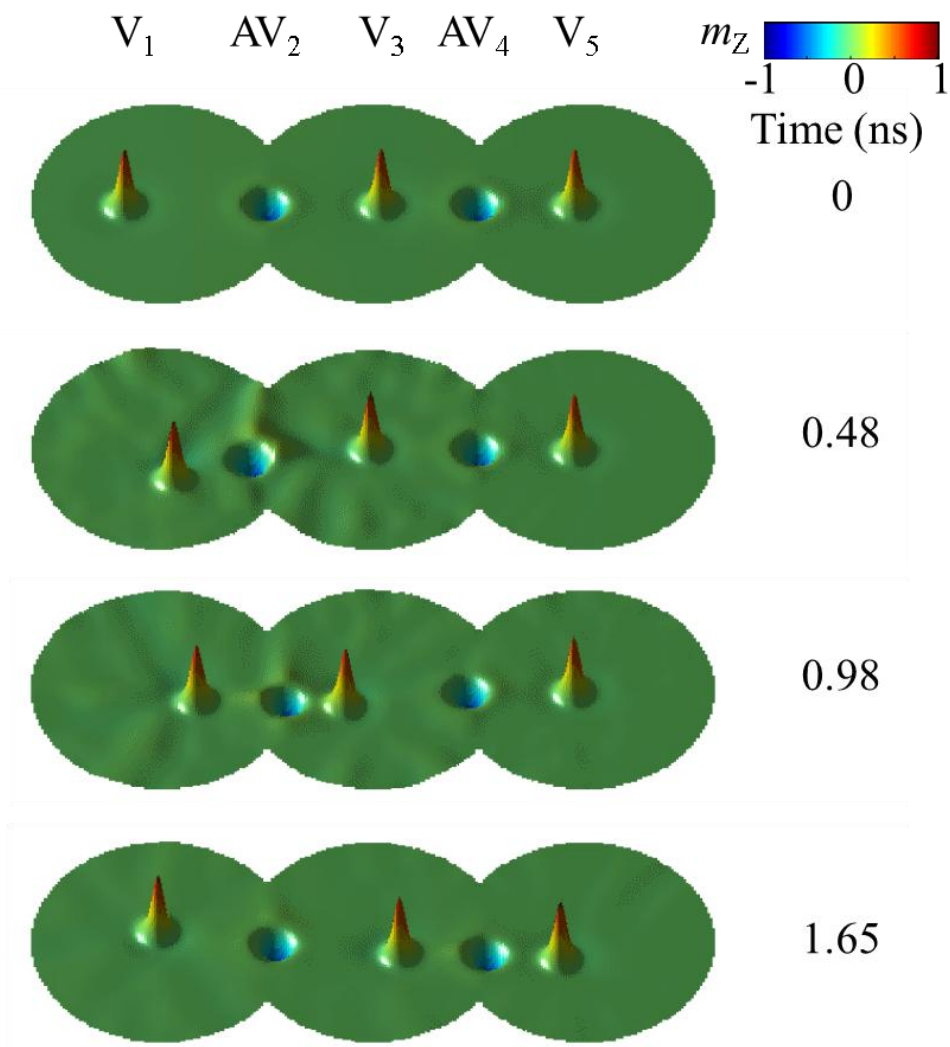

Fig. 3.2 Temporal change of positions of the magnetic vortex cores and antivortex cores.

correspond to $\omega/2\pi$ = 0.23, 0.45, 0.55, 0.98, and 1.11 GHz, respectively, spreading in a wide range from a few hundreds of MHz to the GHz level. Each peak in each frequency spectrum is located at the same corresponding frequency from V_1 through V_5, indicating that there are five distinct modes in the whole system. Because of the intrinsic damping of each core gyration, those peaks are somewhat broadened and overlapped with the neighboring peaks. There are noticeable differences between the vortex and antivortex-core motions: in antivortex motions, that is, in the AV_2 and AV_4 spectra, the ω_3 peak disappears, while in the V_3 spectrum, the ω_2 peak disappears and the ω_4 peak becomes very weak. In order to obtain those data with a better spectral resolution, we carried out further simulations with the same model but with an extremely low damping constant, α = 0.0001. The resultant FFT spectra are shown in the right column of Fig. 3.3 (b). As can be seen, the five major peaks become sharper. The very small subsidiary peaks in the FFT spectra might be associated with higher harmonics and the nonlinear effect of the complex geometric confinements (e.g., the notch-shaped boundaries) or the discreteness of the core positions due to the finite cell size.

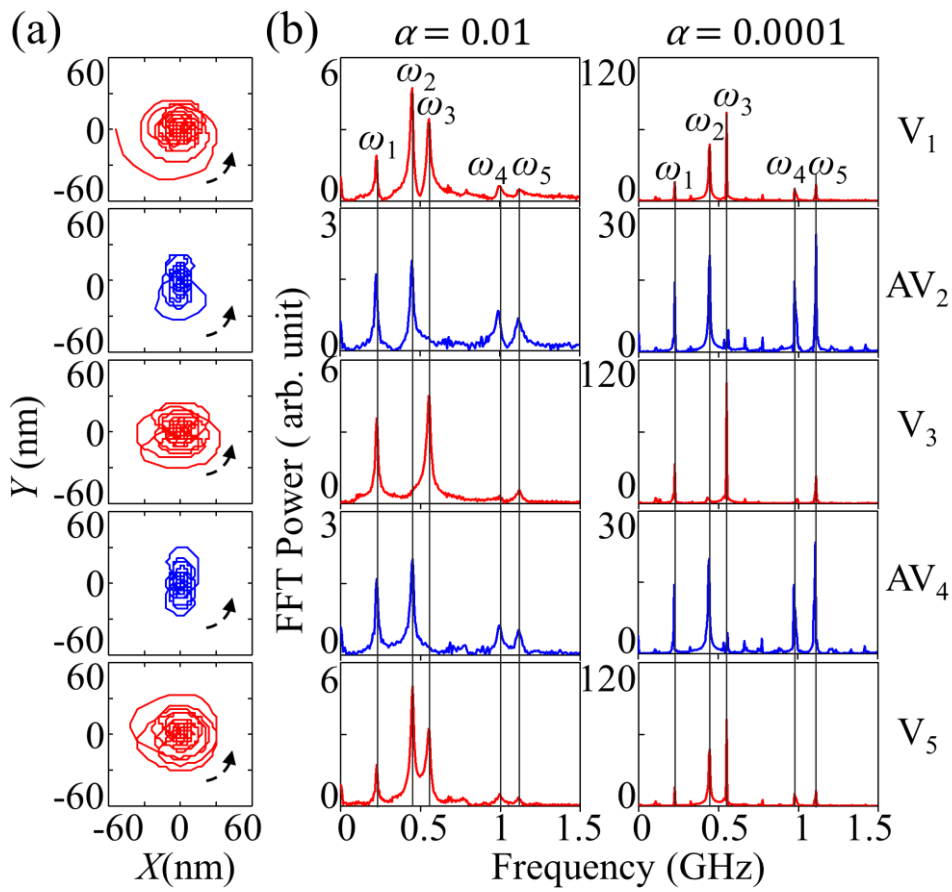

Fig. 3.3 (a) Trajectories of gyration motions of individual vortex cores (red lines) and antivortex cores (blue lines). (b) FFTs of x components of individual core-position vectors from their own center positions. The left (right) column is the result with α = 0.01 (0.0001). The five major peaks are denoted ω_i where i = 1,2,3,4, and 5, and are marked by the gray vertical lines.

3.3 Spatial correlation of eigenmodes of coupled vortex antivortex gyration.

Making inverse FFTs of all of those peaks of each mode with α = 0.0001, we obtained the spatial correlation between the five cores' motion for each mode, as shown in Fig. 3.4 The trajectories of the orbiting cores are compared for all of the modes, along with the corresponding profiles of the *Y* components. The *Y* component profiles are different markedly between the modes. The most noteworthy feature is the fact that the collective core motions show a standing-wave form with a different overall wavelength for a given mode. The orbiting radii of the five cores for a given mode are symmetric with respect to the center of the whole system (i.e., at V_3) and are also completely pinned at the imaginary points at both ends, denoted AV_0 and AV_6, as reported in Refs. 49. The lower ω_1, ω_2, and ω_3 modes and the higher ω_4 and ω_5 modes are quite different in terms of their standing-wave forms. For the ω_1 mode, all of the cores move in phase, while for the ω_2 mode, the core of V_3 acts as a node, and for the ω_3 mode, the two antivortex cores act as standing-wave nodes. For the ω_4 and ω_5 modes, the two antivotices are highly excited relative to the three vortices. Also, the antivortices' core motions are permeated into the bonding axis, thus resulting in higher energy states due to their strong exchange interaction with the neighboring vortices. The difference between the individual modes can be understood by the relative phases between the vortex's and antivortex's effective magnetizations, <**M**>, induced by their own core shifts

and consequently by their dynamic dipolar interaction, as discussed in Ref. 49. The relative phases of the <**M**> between the neighboring core gyrations determine the mode's average dynamic dipolar energy. However, the strong exchange interaction in such a connected thin-film strip must also be taken into account. Due not only to the unknown potential wells of the antivortices but also the complex asymmetric exchange interaction terms between the vortices and antivortices, it is difficult, in such V-AV lattices, to separately extract the individual contributions of the exchange and dipolar interactions to the individual core motions in each mode.

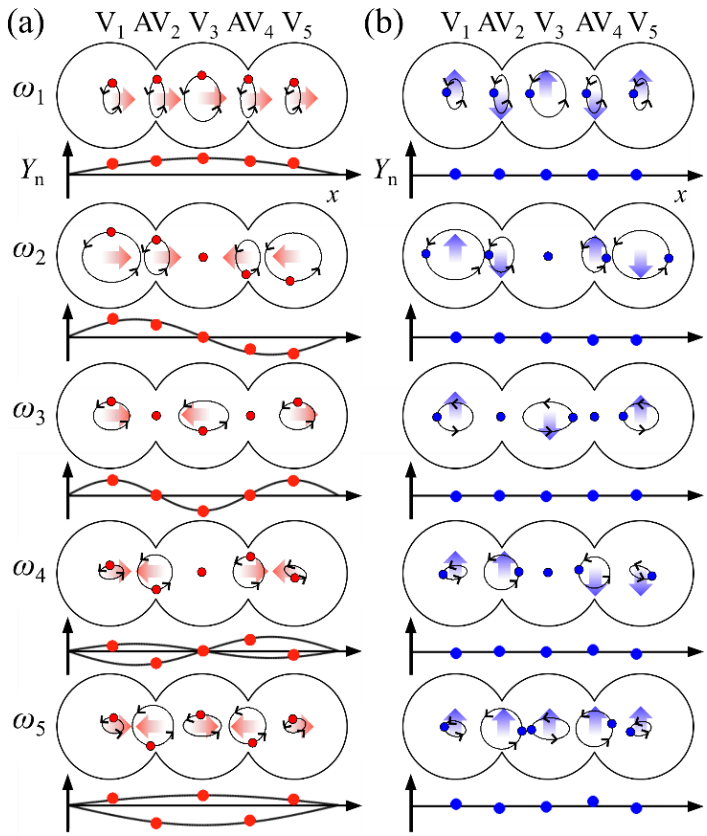

Fig. 3.4 Spatial distributions of individual core positions for five different collective motions (modes). The left and right columns correspond to the core positions taken at *T* and *T*/4 after about 100 ns. The core motions' trajectories are magnified for clear comparison (though the magnifications are different for the different modes). The wide arrows represent the directions of the effective magnetizations <**M**> induced by their own core shifts. The spatial profile of the *Y* components of the core-position vectors for each mode represents a standing wave of a certain wavelength, as displaced by the corresponding solid line.

Chapter4

Collective modes of vortex-antivortex gyration in semi-infinite 1D vortex-antivortex lattices

4.1 Dispersion relation of vortex-antivortex gyration in 1D semi-infinite lattices

On the basis of the findings in the previous chapter, we extended our study to longer chains of periodic arrays of alternating vortices and antivortices, as shown in Fig. 4.1 (a). Here we consider two different polarization orderings with the same CCW chirality for all of the individual vortices: antiparallel and parallel orderings represented by (p_V, p_{AV}) = (+1, -1) and (p_V, p_{AV}) = (+1, +1), respectively. For the V-AV finite lattice, the thickness was set to 40 nm to make it more stable than in a thinner strip and we applied a static local field of 200 Oe in the *-y* direction in the left-end disk. The other simulation conditions were the same as those for the earlier model shown in Fig. 3.1. From the FFTs of the *x* components of all of the 25 core positions, we obtained dispersion curves in the reduced zone scheme for the antiparallel and parallel polarization orderings, as shown in Fig. 4.1 (b). Here, we assume that the interdistance between the neighboring vortices and

antivortices is equal to the average value, $\bar{d}_{\mathrm{int}}/2$ =121 nm, where $\bar{d}_{\mathrm{int}}$ is the lattice constant of a unit basis for V-AV lattices, though there are slight differences in the cores' distances in the center and end regions. The dispersions generally were asymmetric with respect to the wavenumber k=0, because the initial core motion was excited only in the left vortex and was then propagated toward the $+x$ direction. Therefore, the modes with positive group velocities were relatively strong as compared with those with the negative group velocities. In such band structures, there are two distinct higher- and lower-frequency branches, as expected from the two different types of standing-wave forms found in the earlier V-AV model shown in Fig. 3.1. It is noteworthy that such dispersions are quite analogous to collective gyrations in the *acoustic branch* and *optical branch*, respectively, as observed in only vortex-state lattices consisting of alternating different materials[24] or in diatomic lattice vibrations. This indicates that the present 1D V-AV lattice, even with a single soft magnetic material, acts as a bi-material medium. We also note that each branch consists of quantized flat-shaped local modes. In the FFTs of the coupled V-AV gyrations, we applied a periodic boundary condition: as a bi-object array, the wave number is set to $k=\pi m/N\bar{d}_{\mathrm{int}}$, where N is the number of the unit basis, and m is an arbitrary integer in the $-\pi/\bar{d}_{\mathrm{int}} \leq k < \pi/\bar{d}_{\mathrm{int}}$ constraint[52]. At each of the N-discrete k values, there are two corresponding frequencies, thus leading to $2N$ normal modes[24,52].

In both polarization orderings, the bandgap between the two branches is

almost the same, ~0.25 GHz, and the lowest frequency of the higher branches is ~1.23 GHz. The band width of the lower branch is as wide as ~0.9 GHz, due to the strong exchange-dipole interaction between vortices and antivortices in such connected-disk arrays. The overall shape of the lower branch is concave up; that is, the frequency is lowest at k=0 and highest at the first Brillion zone boundary, k=k_{BZ} = $\pi / \bar{d}_{int}$, for both polarization orderings. However, the shape of the higher branch varies according to the polarization ordering: concave down for the antiparallel polarization ordering, and almost flat for the parallel one. In the lower branch, as k approaches the k_{BZ}, the ω value reaches the angular eigenfrequency ω_0 of isolated Py disks of the given dimensions (here $\omega/2\pi$ = 0.97 GHz). This result reveals that all of the antivortices act as nodes in the standing-wave form, and thus do not contribute to the lower band at $k = k_{BZ}$ but dominantly contribute to the higher band at $k = k_{BZ}$. The flat higher band for the parallel polarization ordering is owed to the fact that the dynamic interaction energy averaged over one cycle of gyration is almost equal for the entire k range. The ω value in the higher flat band would provide the angular eigenfrequency of a virtual system composed of isolated antivortices (here ~1.23 GHz).

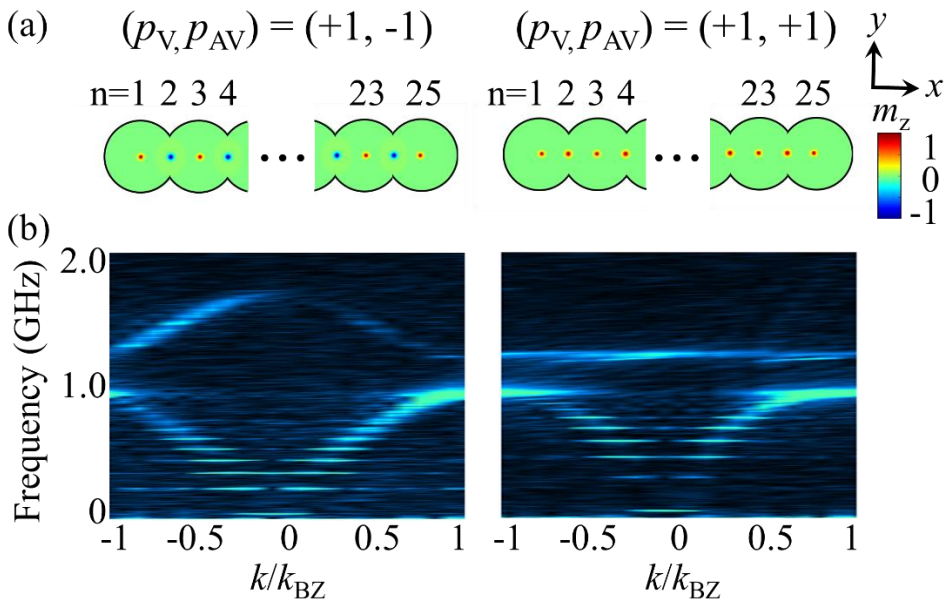

Fig. 4.1 (a) Model geometry of 1D chains comprising 13 vortices and 12 antivortices between the neighboring vortices. The left and right columns correspond to the antiparallel (p_V ,p_{AV} = 1, - 1) and parallel (p_V , p_{AV} = +1) polarization orderings, respectively. Odd (even) index numbers from 1 to 25 represent vortices (antivortices). The in-plane curling magnetization of all of the vortices is CCW. The red (blue) dots display upward (downward) core orientation. (b) Dispersions of collective V-AV gyration modes in given V-AV-V chains. FFT spectra were obtained from the *x* components of the core positions using the zero-padding technique for a sufficient *k*-space resolution of 1.4×10^6 m^{-1}. The results are plotted in the reduced zone scheme.

4.2 Perpendicular bias field effect on dispersion relation

Next, in order to control the observed two-branch band structure and the gyration-signal propagation speed in such V-AV lattices, we applied perpendicular bias fields H_z of different strength and direction. It is known that the eigenfrequency of a gyrotropic mode of vortices varies with H_z, as expressed by $\omega = \omega_0(1 + pH_z / H_s)$, with ω_0 the angular eigenfrequency at $H_z = 0$, and H_s the perpendicular field for the saturation of a given system's magnetization[53, 54]. In order to clarify the perpendicular field dependence of ω_0 of isolated antivortex, we conducted additional numerical calculation. In our numerical calculations, we used asteroid model geometry where isolate antivortex is metastable as shown in Fig. 4.2 (a). The lateral size was 300nm and the thickness was 20nm. The circular edges had a radius of 144nm. We used same material parameters of permalloy that used in previous simulation. Additionally, the uniform perpendicular field with respect to the asteroid-shaped thin film, the strength varied from -2 kOe to 2 kOe with the intervals of 1 kOe. The antivortex core was displaced by applying in-plane field of 200 Oe in the $+x$ direction. Upon turning off the in-plane field, we monitored temporal variation of x component of magnetization (M_x) induced by the core gyration. Fig 4.2 (b) shows the eigenfrequencies of the isolated antivortex under various H_z, obtained from the FFT of the variation of Mx. In this result, ω_0 was estimated to be linearly proportional to H_z as well. Thus, it is interesting to examine how coupled gyrations in such V-AV lattices, and consequently how the resultant band structure, varies with H_z. In our further simulations, we excited vortex

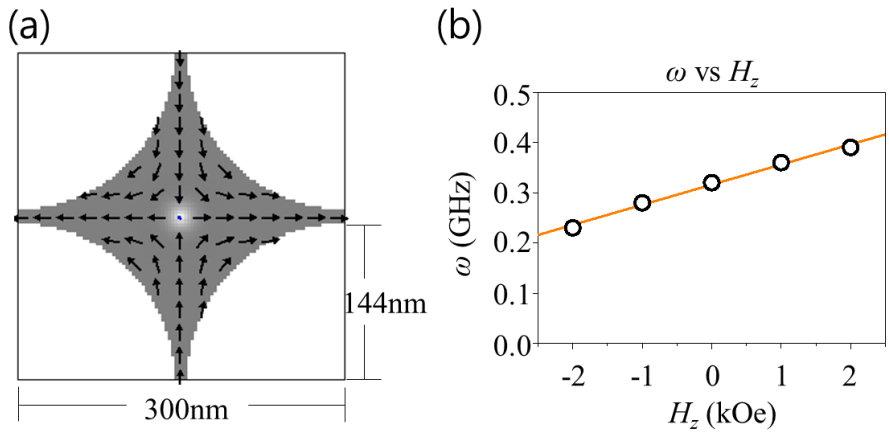

Fig. 4.2 (a) Model geometry of isolated antivortex in the asteroid shape. (b) Eigenfrequencies of isolated antivortex gyration under perpendicular field bias.

and antivortex gyrations by the same method as mentioned in the chapter 4.1, but under the application of different values of H_z at intervals of 1 kOe in the $H_z = -3 - +3$ kOe range. Figure 4.3 compares the contrasting band structures for the indicated H_z values. The band widths of the lower and higher bands and their bandgaps markedly vary with H_z and differ from the parallel to antiparallel polarization ordering. For example, at H_z = -3.0 kOe, in the case of (p_V, p_{AV}) = (+1, +1), the higher flat band becomes stronger and more flat over a wide range of k, and the lower band becomes weak, while in the case of (p_V, p_{AV}) = (+1, -1), the higher flat band becomes very weak and the lower band becomes relatively strong. Also in the case of (p_V , p_{AV}) = (+1, +1), the lower band width increases with H_z, while in the case of (p_V , p_{AV}) = (+1, -1) it increases with H_z until H_z = 1 kOe and then decreases again.

We also plotted the angular frequencies ω_{BZ} at k=k_{BZ} for the lower and higher bands (see left of Fig. 4.4). As for (p_V , p_{AV}) = (+1, +1), ω_{BZ} of the lower and the higher bands are linearly proportional to H_z in the given H_z range, with slopes of 0.12 GHz/kOe and 0.21 GHz/kOe, respectively. In fact, ω_{BZ} for the higher and lower bands correspond to ω_0's of the isolated antivortex and vortex, respectively. Thus, the linear dependences of ω_{BZ} on H_z for both bands are associated with the variation of the ω_0 of isolated vortices and antivotices with H_z, as expressed by $\omega = \omega_0(1 + pH_z / H_s)$. Using this equation, linear fits to the data yield the two fitting parameters: $\omega_0/2\pi$ = 0.95 ± 0.002 (GHz), H_s = 8.2 ± 0.08 (kOe)

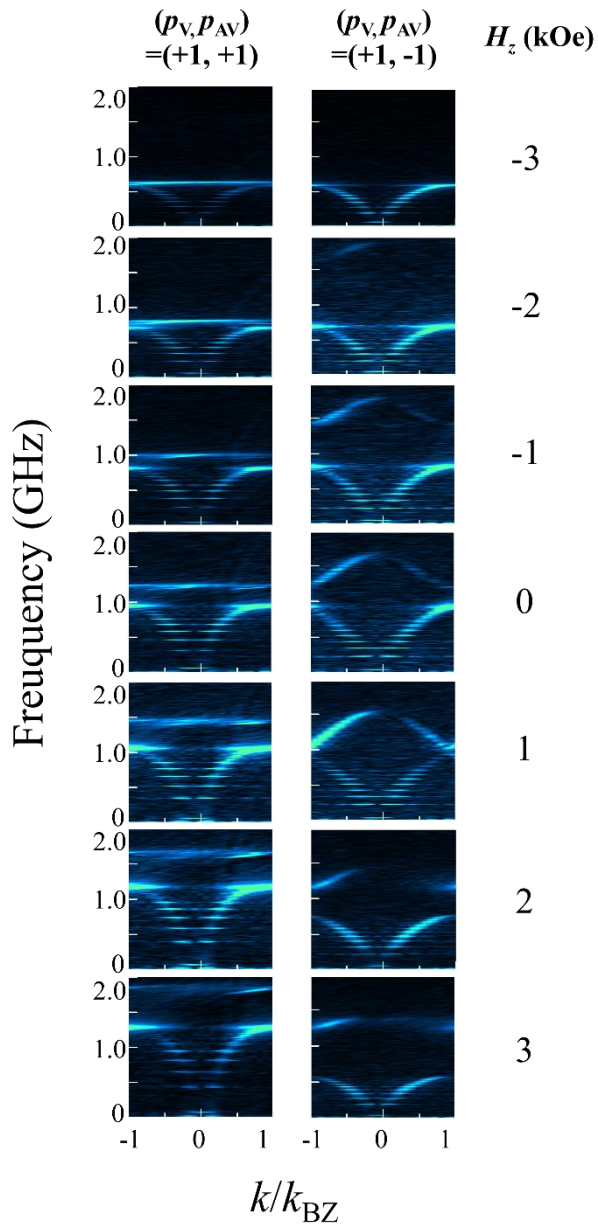

Fig. 4.3 Two-branch band-structure variation with H_z for both parallel and antiparallel polarization orderings in V-AV lattice shown in Fig. 4.1 (a).

for the lower band and $\omega_0/2\pi$ = 1.2 ± 0.004 (GHz), H_s = 5.9 ± 0.01 (kOe) for the higher band. These two values of $\omega_0/2\pi$ = 0.95 and 1.2 GHz are close to the ω_0 of isolated vortices and antivortices. The larger slope for the higher band is the result of the higher ω_0 and lower H_s . In the case of (p_V , p_{AV}) = (+1, -1), on the other hand, the ω_{BZ} of the higher band is linearly decreased and then, after crossing about H_z = 1 kOe, increased, as shown in the right panel of Fig. 4.4. The ω_{BZ} of the lower band, meanwhile, shows exactly the reverse effect. The higher (lower) band in the H_z < 1 kOe range seems to follow the relation $\omega = \omega_0(1 - H_z / H_s)$ ($\omega = \omega_0(1 + H_z / H_s)$), whereas in the H_z > 1 kOe range, $\omega = \omega_0(1 + H_z / H_s)$ ($\omega = \omega_0(1 - H_z / H_s)$). These results reveal that in the H_z < 1 kOe (H_z > 1kOe) range, antivortices play a dominant role in the higher (lower) band and that vortices do the same in the lower (higher) band. That is why the band-structure variation with H_z is rather more complicated in the case of (p_V , p_{AV}) = (+1, -1) than in the case of (p_V , p_{AV}) = (+1, +1).

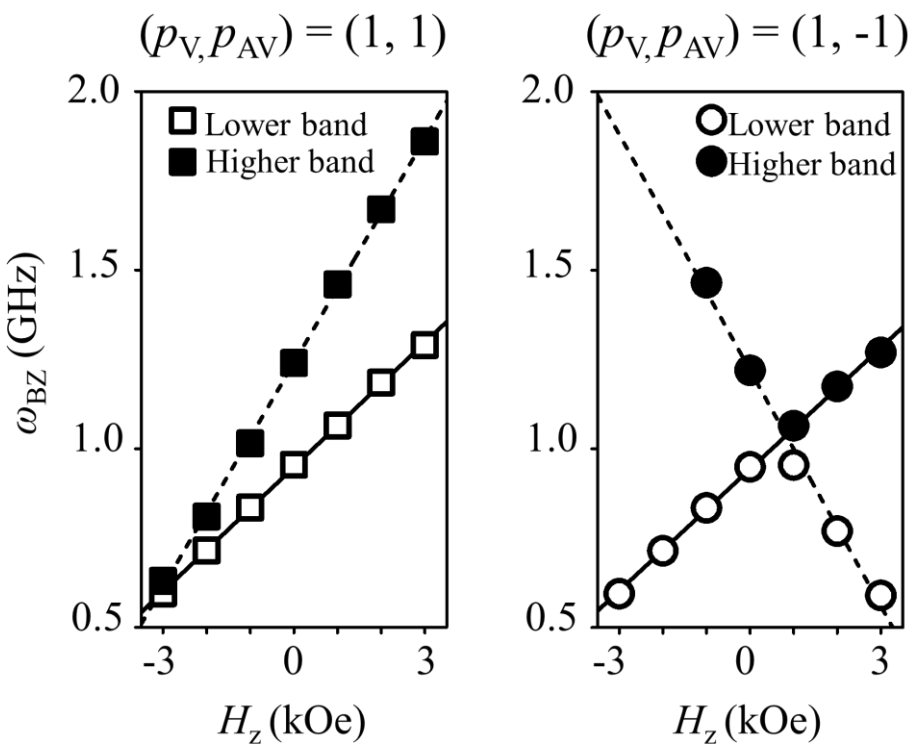

Fig. 4.4 Plots of angular frequency at $k=k_{BZ}$ for lower and higher bands in both polarization ordering cases. The solid and dashed lines represent the results of linear fits to the data.

4.3 Perpendicular bias field effect on gyration-signal propagation speed

From the technological perspective, as with domain-wall motions in a given nanostrip, gyration-signal propagation through alternating V-AV lattices can be used as an information carrier. From displacements of the individual cores from their own center positions in the whole system with time, we estimated the gyration-signal propagation speeds versus H_z for both polarization ordering cases. Fig. 4.5(a) shows that the resultant propagation speed is linearly proportional to H_z in the given H_z range for the parallel polarization ordering (open squares), but that for the antiparallel ordering (open circles), the speed decreases with increasing $|H_z|$ and, thereby, is at the maximum at H_z=0. The speed difference ratio between the parallel and antiparallel orderings increases markedly with H_z, as shown in Fig. 4.5(b). For example, the difference ratio (speed of (p_V, p_{AV}) = (+1, +1) - speed of (p_V, p_{AV}) = (+1, -1))/ speed of (p_V, p_{AV}) = (+1, -1)) increases to ~135% at H_z = 3 kOe, compared with 28% at H_z = 0 and 2% at H_z = - 3 kOe. This remarkable variation of the speed difference ratio with H_z is the result of increases in the intrinsic ω_0's of both the vortex and antivortex with H_z for (p_V, p_{AV}) = (+1, +1) and the result of decreases in the antivortex's ω_0 for (p_V, p_{AV}) = (+1, -1). These results are very promising from the technological point of view, owing to the following several advantages of this signal-propagation mechanism and its applicability to any potential spin-based signal-processing devices: 1) such V-AV lattices can be

made of simple, single-material, round-shaped modulated nanostrips; 2) the parallel polarization ordering between neighboring vortices and antivortices is readily available by application of H_z ; 3) such faster gyration-propagation speed is caused by the combined exchange and dipolar coupling between the neighboring vortices and antivortex, and accordingly the propagation speed is higher than 1 km/sec and controllable by the application of H_z.

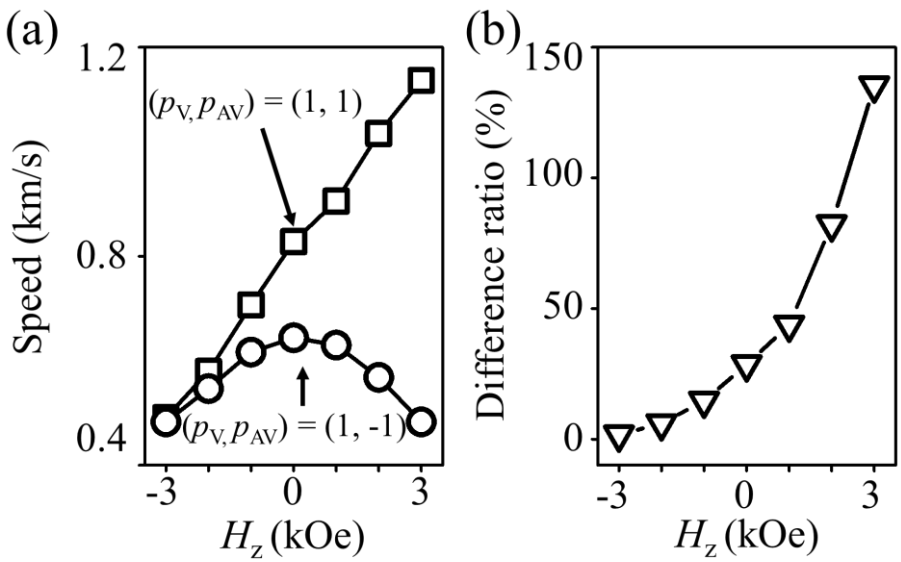

Fig. 4.5 (a) Gyration-signal propagation speed in both polarization ordering cases and (b) their difference ratio.

Chapter 5

Conclusion

In summary, we studied the dynamics of coupled vortices and antivortices in their alternating 1D periodic arrays. Standing-wave discrete modes and their dispersion relations were found to have lower and higher branches. We found faster gyration-signal propagations in continuous nanostripes composed of alternating vortex and antivortex lattices for the parallel polarization ordering than for the antiparallel one; both are much faster than only-vortex-state arrays. Also, the band structures and gyration-propagation speed are markedly variable by means of the perpendicular bias field. Such core-gyration signals can be detectable due to relatively large variations in the in-plane magnetizations of vortex and antivortex motions. This work provides not only fundamental insights into the dynamic interactions between different types of topological solitons but a robust means for significant enhancements of gyration-signal propagation speed in soft magnetic thin-film nanostrips.

Bibliography

[1] S. Bandyopadhyay and M. Cahay, *Electron spin for classical information processing: a brief survey of spin-based logic devices, gates and circuits*, Nanotechnology, **20**, 412001 (2009).

[2] S. S. P. Parkin, M. Hayashi, and L. Thomas, *Magnetic Domain-Wall Racetrack Memory*. Science, **320**, 190 (2008).

[3] Y. Huai, *Spin-Transfer Torque MRAM (STT-MRAM): Challenges and Prospects*, AAPPS Bulletin **18** No. 6, 33. (2008)

[4] V. V. Kruglyak, S. O. Demokritov, and D. Grundler, *Magnonics*, J. Phys. D: Appl. Phys. **43**, 264001 (2010).

[5] A. A. Serga, A. V. Chumak, and B. Hillebrands, *YIG magnonics*, J. Phys. D: Appl. Phys. **43**, 264002 (2010)

[6] S.-K. Kim, *Micromagnetic computer simulations of spin waves in nanometre-scale patterned magnetic elements*, J. Phys. D: Appl. Phys. **43**, 264004 (2010).

[7] S. Neusser and D. Grundler, *Magnonics: Spin Waves on the Nanoscale*, Adv. Mater. **21**, 2927 (2009).

[8] K. Y. Guslienko, B. A. Ivanov, V. Novosad, Y. Otani, H. Shima, and K. Fukamichi, *Eigenfrequencies of vortex state excitations in magnetic submicron-size disks*, J. Appl. Phys. **91**, 8037 (2002).

[9] S. Kasai, Y. Nakatani, K. Kobayashi, H. Khono, and T. Ono, *Current-Driven Resonant Excitation of Magnetic Vortices*, Phys. Rev. Lett. **97**, 107204 (2006).

[10] V. S. Pribiag, I. N. Krivorotov, G. D. Fuchs, P. M. Braganca, O. Ozatay, J. C. Sankey, D. C. Ralph, and R. A. Buhrman , *Magnetic vortex oscillator driven by d.c. spin-polarized current*, Nat. Phys. **3**, 498 (2007).

[11] S. Petit-Watelot, J. Kim, A. Ruotolo, R. M. Otxoa, K. Bouzehouane, J.Grollier, A. Vansteenkiste, B. Van de Wiele, V. Cros, and T. Devolder, *Commensurability and chaos in magnetic vortex oscillations*, Nat. Phys. **8**, 682 (2012).

[12] B. Van Waeyenberge, A. Puzic, H. Stoll, K. W. Chou, T. Tyliszczak, R. Hertel, M. Fähnle, H. Brückl, K. Rott, G. Reiss, I. Neudecker, D. Weiss, C. H. Back and G. Schütz, *Magnetic vortex core reversal by excitation with short bursts of an alternating field*, Nature **444**, 461 (2006).

[13] R. Hertel, S. Gliga, M. Fähnle, and C. M. Schneider, *Ultrafast Nanomagnetic Toggle Switching of Vortex Cores*, Phys. Rev. Lett. **98**, 117201 (2007).

[14] S. Bohlens, B. Krüger, Drews, M. Bolte, G. Meier, and D. Pfannkuche, *Current controlled random-access memory based on magnetic vortex handedness*, Appl. Phys. Lett. **93**, 142508 (2008).

[15] Y.-S. Yu, H. Jung, K.-S. Lee, P. Fischer, and S.-K. Kim, *Memory-bit selection and recording by rotating fields in vortex-core cross-point architecture* Appl. Phys. Lett. **98**, 052507 (2011).

[16] S. Barman, A. Barman, and Y. Otani, *Dynamics of 1-D Chains of Magnetic Vortices in Response to Local and Global Excitations*, IEEE Trans. Magn. **46**, 1342 (2010).

[17] H. Jung, K.-S. Lee, D.-E. Jeong, Y.-S. Choi, Y.-S. Yu, D.-S. Han, A. Vogel, L. Bocklage, G. Meier, M.-Y. Im, P. Fischer, and S.-K. Kim, *Tunable negligible-loss energy transfer between dipolar-coupled magnetic disks by stimulated vortex gyration*, Sci. Rep. **1**, 59; DOI:10.1038/srep00059 (2011).

[18] H. Jung, Y.-S. Choi, K.-S. Lee, D.-S. Han, Y.-S. Yu, M.-Y. Im, P. Fischer, and S.-K. Kim, *Logic Operations Based on Magnetic-Vortex-State Networks*, ACS Nano **6**, 3712 (2012).

[19] A. Dussaux , B. Georges, J. Grollier, V. Cros, A.V. Khvalkovskiy , A. Fukushima, M. Konoto, H. Kubota, K. Yakushiji, S. Yuasa, K.A. Zvezdin, K. Ando & A. Fert, *Large microwave generation from current-driven magnetic vortex oscillators in magnetic tunnel junctions*. Nat. Commun, **1**, 8 Nat. Commun. 1, 8 (2010)

[20] A. Ruotolo, V. Cros, B. Georges, A. Dussaux, J. Grollier, C. Deranlot, R. Guillemet, K. Bouzehouane, S. Fusil, and A. Fert, *Phase-locking of magnetic vortices mediated by antivortices*, Nat. Nanotechnol. **4**, 528 (2009).

[21] B. Krüger, A. Drews, M. Bolte, U. Merkt, D. Pannkuche, and Guido Meier, *Vortices and antivortices as harmonic oscillators*, J. Appl. Phys. **103**, 07A501

(2008)

[22] S. Barman, A. Barman, and Y. Otani, *Controlled propagation of locally excited vortex dynamics in linear nanomagnet arrays*, J. Phys. D: Appl. Phys. **43**, 335001 (2010).

[23] A. Vogel, M. Martens. M. Weigand and Guido Meier, *Signal transfer in a chain of stray-field coupled ferromagnetic squares*, Appl. Phys. Lett. **99**, 042506 (2011).

[24] D.-S Han, H.-B. Jeong, and S.-K. Kim, *Contrasting vortex-gyration dispersions for different lattice bases in one-dimensional magnetic vortex arrays*, Appl. Phys. Lett. **103**, 112406 (2013).

[25] H. Wang and C. E. Campbell, *Spin dynamics of a magnetic antivortex: Micromagnetic simulations*, Phys. Rev. B **76**, 220407(R) (2007).

[26] S. Gliga, M. Yan, R. Hertel, and C. M. Schneider, *Ultrafast dynamics of a magnetic antivortex: Micromagnetic simulations*, Phys. Rev. B **77**, 060404(R) (2008).

[27] T. Kamionka, M. Martens, K. W. Chou, M. Curcic, A. Drews, G. Schütz, T. Tyliszczak, H. Stoll, B. V. Waeyenberge, and G. Meier, *Magnetic Antivortex-Core Reversal by Circular-Rotational Spin Currents*, Phys. Rev. Lett. **105**, 137204 (2010).

[28] K. Shigeto, T. Okuno, K. Mibu, T. Shinjo, and T. Ono, *Magnetic force*

microscopy observation of antivortex core with perpendicular magnetization in patterned thin film of permalloy, Appl. Phys. Lett. **80**, 4190 (2002).

[29] M. Pues, M. Martens, T. Kamionka, and G. Meier, *Reliable nucleation of isolated magnetic antivortices*, Appl. Phys. Lett. **100**, 162404 (2012).

[30] V. L. Mironov, O. L. Ermolaeva, S. A. Gusev, A. Y. Klimov, V. V. Rogov, B. A. Gribkov, O. G. Udalov, A. A. Fraerman, R. Marsh, C. Checkley, R. Shaikhaidarov, and V. T. Petrashov, *Antivortex state in crosslike nanomagnets*, Phys. Rev. B **81**, 094436 (2010).

[31] A. Haldar and K. Buchanon. *Magnetic antivortex formation in pound-key-like nanostructures* Appl. Phys. Lett. **102**, 112401 (2013).

[32] Craik, D. J., and R. S. Tebble, *Feromagnetism and Ferromagnetic Domains* (North Holland, Amsterdam, 1965).

[34] J. Miguel, J. Sanchez-Barriga, D. Bayer, J. Kurde, B. Heitkamp, M. Piantek, F. Kronast, M. Aeschlimann, H. A. Durr, and W. Kuch, *Time-resolved magnetization dynamics of cross-tie domain walls in permalloy microstructures*, J. Phys.: Condens. Mattter **21**, 496001 (2009).

[35] C. E. Zaspel, *Phase locking of vortex-based spin-torque nanocontact oscillators by antivortices*. Appl. Phys. Lett. **102**, 052403 (2013).

[36] W. F. Brown Jr., *Micromagnetics*, Wiley-Interscience (1963)

[37] L. D. Landau and E. M. Lifshitz, *On the theory of the dispersion of magnetic permeability in ferromagnetic bodies*, Phys. Z. Sowjetunion **8**, 153 (1935);

[38] T. L. Gilbert, A Lagrangian formulation of the gyromagnetic equation of the magnetic field Phys. Rev. **100**, 1243 (1955).

[39] K.S. Lee, Ph.D. thesis, Seoul National University, South Korea (2010).

[40] See http://math.nist.gov/oommf for more information about the code.

[41] A. Wachowiak, J. Wiebe, M. Bode, O. Pietzsch, M. Morgenstern, and R. Wiesendanger, *Direct Observation of Internal Spin Structure of Magnetic Vortex Cores*, Science, **298**, 577 (2002).

[42] T. Shinjo, T. Okuno, R. Hassdorf, K. Shigeto, T. Ono, *Magnetic Vortex Core Observation in Circular Dots of Permalloy*, **289**, 930 Science (2000)

[43] A. Drews, *Dynamics of magnetic vortices and antivortices*, Ph.D. thesis, Universität Hamburg (2009)

[44] A. A. Thiele, *Steady-State Motion of Magnetic Domains*, Phys. Rev. Lett. **30**, 230 (1973).

[45] D. L. Huber, *Dynamics of spin vortices in two-dimensional planar magnets*, Phys. Rev. B **26**, 3758 (1982)

[46] J. Shibata, K. Shigeto, and Y. Otani, *Dynamics of magnetostatically coupled vortices in magnetic nanodisks*, Phys. Rev. B **67**, 224404 (2003).

[47] H. Jung, Y.-S. Yu, K.-S. Lee, M.-Y. Im, P. Fischer., L. Bocklage, A. Vogel, M. Bolte, G. Meier and S.-K. Kim, *Observation of coupled vortex gyrations by 70-ps-time- and 20-nm-space-resolved full-field magnetic transmission soft x-ray microscopy*, Appl. Phys. Lett. **97**, 222502 (2010).

[48] A. Vogel, M. Martens. M. Weigand and Guido Meier, *Signal transfer in a chain of stray-field coupled ferromagnetic squares*, Appl. Phys. Lett. **99**, 042506 (2011).

[49] D.-S. Han, A. Vogel, H. Jung. K.-S. Lee, M. Weigand, H. Stoll, G. Schütz, P. Fischer, G. Meier, and S.-K. Kim, *Wave modes of collective vortex gyration in dipolar-coupled-dot-array magnonic crystals*, Sci. Rep. **3**, 2262; DOI:10.1038/srep02262 (2013).

[50] N. Wiese, S. McVitie, J. N. Chapman, A. Capella-Kort and F. Otto, *On the scaling behaviour of cross-tie domain wall structures in patterned NiFe elements*, EPL **80** 57003 (2007).

[51] J. Li, A. Tan, K. W. Moon, A. Doran, M. A. Marcus, A. T. Young, E. Arenholz, S. Ma1, R. F. Yang, C. Hwang and Z. Q. Qiu, *Stabilizing a magnetic vortex/antivortex array in single crystalline Fe/Ag(001) microstructures*, Appl. Phys. Lett. **104**, 262409 (2014).

[52] N. W. Ashcroft and N. D. Mermin, *Solid State Physics*, (Thomson Learning, Inc., London, 1976).

[53] G. de Loubens, A. Riegler, B. Pigeau, F. Lochner, F. Boust, K. Y. Guslienko, H. Hurdequint, L. W. Molenkamp, G. Schmidt, A. N. Slavin, V. S. Tiberkevich, N. Vukadinovic, and O. Klein, *Bistability of Vortex Core Dynamics in a Single Perpendicularly Magnetized Nanodisk*, Phys. Rev. Lett. **102**, 177602 (2009).

[54] M.-W. Yoo, K.-S. Lee, D.-S. Han and S.-K. Kim, *Perpendicular-bias-field-dependent vortex-gyration eigenfrequency*, J. Appl. Phys. **109,** 063903 (2011).

Publication List

1	**H.-B Jeong** and S.-K Kim, *Enhanced gyration-signal propagation speed in one-dimensional vortex-antivortex lattices and its control by perpendicular bias field*. Appl. Phys. Lett. (2014)
2	D.-S Han, **H.-B. Jeong** and S.-K. Kim, *Contrasting vortex-gyration dispersions for different lattice bases in one-dimensional magnetic vortex arrays*, Appl. Phys. Lett. **103**, 112406 (2013)
3	D.-S. Han, Y.-J. Cho, **H.-B. Jeong**, S.-K. Kim, *Perpendicular-bias-field control of coupled-vortex oscillations in nanodot networks*, (submitted)

초 록

1 차원 자기 소용돌이-반소용돌이 격자에서 발생하는 회전운동에 관한 연구

최근에 차세대 정보처리소자의 후보로 자기소용돌이 배열의 동적 거동이 연구되고 있다. 미래의 소자에서 필요로 하는 특성 중 하나는 빠른 작동속도이다. 하지만 물리적으로 떨어져 있는 자기소용돌이들의 배열을 이용한 기존 연구에서는 신호전달 속도가 다른 후보들에 비해 상대적으로 낮았다.

본 논문에서는, 디스크들이 물리적으로 붙어있어 자기소용돌이와 자기반소용돌이가 차례로 나타나는 구조를 도입하였다. 이 경우 두 자화구조가 쌍극자 상호작용 뿐만 아니라 교환상호작용을 통해 강하게 결합된다. 본 연구에서는 결합된 자기소용돌이-반소용돌이 배열에서 핵의 회전운동의 전파에 의한 신호전달 현상을 발견하였으며, 핵의 집단적 진동운동이 정상파로 표현되는 기본모드들로 구성되어 있다는 것을 밝혀내었다. 그리고 핵의 진동운동의 밴드구조가 두 갈래로 존재하는 것을 확인하여 자기소용돌이-반소용돌이 배열의 동적 거동이 이원자격자의 진동운동과 유사한 것을 확인하였다.

본 연구에서는 또한 수직자기장을 인가하여 의해 핵의 회전운동의 전파속도를 조절할 수 있다는 것을 입증하였고 전파속도는 최대 1km/s 가 넘는 빠른 속도를 기록하였다.

본 연구는 결합된 자기소용돌이-반소용돌이 간의 동적 거동의 기초적인 이해 및 이를 이용한 빠른 신호전달 방법을 제공한다. 또한 가는 나노박막을 이용한 정보 전달 매체의 효과적인 속도 향상 방법을 제시한다.

주요어: 자기소용돌이, 자기반소용돌이, 마그논 결정, 신호전달

학번: 2012-23152